Zhen Zhang (张珍), **Shuran Ye** (叶舒然), 🆔 **Bo Yin** (银波), et al.

View Online   Export Citation   CrossMark

ARTICLES YOU MAY BE INTERESTED IN

Machine learning methods for turbulence modeling in subsonic flows around airfoils
Physics of Fluids **31**, 015105 (2019); https://doi.org/10.1063/1.5061693

Feature selection and processing of turbulence modeling based on an artificial neural network
Physics of Fluids **32**, 105117 (2020); https://doi.org/10.1063/5.0022561

An interpretable framework of data-driven turbulence modeling using deep neural networks
Physics of Fluids **33**, 055133 (2021); https://doi.org/10.1063/5.0048909

Call For Papers!

AIP Advances

SPECIAL TOPIC: Advances in Low Dimensional and 2D Materials

A semi-implicit discrepancy model of Reynolds stress in a higher-order tensor basis framework for Reynolds-averaged Navier–Stokes simulations

View Online   Export Citation   CrossMark

Zhen Zhang (张珍),[1,2] Shuran Ye (叶舒然),[1,2] Bo Yin (银波),[1,2] (iD) Xudong Song (宋旭东),[3]
Yiwei Wang (王一伟),[1,2,4,a)] (iD) Chenguang Huang (黄晨光),[1,2,4] and Yaosong Chen (陈耀松)[3]

AFFILIATIONS

[1] Key Laboratory for Mechanics in Fluid Solid Coupling Systems, Institute of Mechanics, Chinese Academy of Sciences, Beijing 100190, China
[2] School of Engineering Science, University of Chinese Academy of Sciences, Beijing 100049, China
[3] College of Engineering, Peking University, Beijing 100871, China
[4] School of Future Technology, University of Chinese Academy of Sciences, Beijing 100049, China

[a)] Author to whom correspondence should be addressed: wangyw@imech.ac.cn

ABSTRACT

With the rapid development of artificial intelligence, machine learning algorithms are becoming more widely applied in the modification of turbulence models. In this paper, with the aim of improving the prediction accuracy of the Reynolds-averaged Navier–Stokes (RANS) model, a semi-implicit treatment of Reynolds stress anisotropy discrepancy model is developed using a higher-order tensor basis. A deep neural network is constructed and trained based on this discrepancy model. The trained model parameters are embedded in a computational fluid dynamics solver to modify the original RANS model. Modification computations are performed for two cases: one interpolation and one extrapolation of different Reynolds numbers. For these two cases, the ability of the modified model to capture anisotropic features has been improved. Moreover, when compared with the mean velocity of large eddy simulations (LES), the root mean square error of the modified model is significantly lower than the original RANS model. Meanwhile, the modified model can better simulate flow field separation and fluctuation in the shear layer and has better prediction accuracy for the reattachment point and the mean velocity profile compared with the original RANS model. In addition, the modified model also improves the prediction accuracy for the mean pressure coefficient and mean friction coefficient of the underlying wall surface. The previously trained model is also directly performed for the modification computation of the two massive separation periodic hill flows. It is shown that the results simulated by the modified model and LES approach are more consistent in both trend and magnitude than the original RANS model and LES approach.

I. INTRODUCTION

Solving the Reynolds-averaged Navier–Stokes (RANS) equations remains an effective and practical approach in engineering applications because this approach only computes the mean flow and omits the turbulent fluctuation of each scale, which reduces the spatial and temporal resolution and shortens the computation period.[1,2] However, in the RANS approach, the effect of the turbulent fluctuation in the mean flow field, that is, the Reynolds stress, is unknown. The eddy-viscosity (turbulent-viscosity) models are often established to close the equations.[3–5] The widely used eddy-viscosity models generally assume a linear relationship between the Reynolds stress and the mean strain rate tensor, which cannot adequately capture anisotropies in the flow field.[6,7] Although higher-order eddy-viscosity models can provide better prediction accuracy, the underlying structure of these models lacks an adequate theoretical basis. Furthermore, there are no rigorous results regarding their convergence.[8] With the availability of high-performance

computing architectures, high-fidelity direct numerical simulation (DNS) and large eddy simulation (LES) can be performed more readily.[9] Moreover, if a machine learning method is combined with the RANS approach and high-fidelity/experimental data are used as the training dataset, it should be possible to construct a more complex relationship between the mean flow field and the level of turbulent fluctuations. This has therefore become a topic of great importance in research on RANS turbulence models.[10–12]

In the past few years, machine learning algorithms have been extensively introduced into turbulence modeling aiming to speed up the computation and enhance existing solvers.[13–20] Ling and Templeton[21] investigated the impact of database size on the performance of random forest machine models. Their results showed that the choice and size of the training database are critical to the performance of the machine learning model. Ling et al.[22] and Ling, Jones, and Templeton[23] further showed that embedding rotational invariants into machine learning models is essential for achieving high-performance predictions. The main purpose of modeling based on machine learning algorithms is to balance efficiency and accuracy. However, interpretability is necessary when modeling physical systems.[9] Consequently, the key work of Ling, Kurzawski, and Templeton[13] proposed a network structure that embeds Galilean invariance in neural network prediction on the basis of a higher-order eddy-viscosity model proposed by Pope.[24] This framework was tensor-based to ensure the Galilean invariance of the predicted model. In addition, based on the work of Ling, Kurzawski, and Templeton,[13] Zhang et al.[25] improved the network structure to predict the Reynolds stress of a channel flow for different Reynolds numbers. The results showed that the Reynolds stress can be accurately reconstructed and predicted. Although the tensor basis neural network (TBNN) improves the prediction capability of the RANS model, the actual training is difficult, which results in difficulties in practical applications.

Scholars also studied data-driven turbulence closure models within the physics-based LES framework to learn the subgrid-scale (SGS) stress. Gamahara and Hattori[26] established a model for finding the relation between the grid-scale flow and the SGS stress tensor using artificial neural networks (ANNs), but this approach did not consider the consumption of the stress tensor form. Pawar et al.[27] presented a model with multilayer ANNs, which utilized coarse-grained field variables to estimate the SGS stress for Kraichnan turbulence. The improvement in the prediction of SGS stresses is achieved in their study. Besides, for LES, the turbulence modeling approach by learning closure terms and making predictions was also documented in Beck, Flad, and Munz[28] and Weatheritt and Sandberg.[29] However, most of the above-mentioned SGS stress model is expressed as an explicit source term in the equation, which leads to the greatly impaired prediction ability of the data-driven model. Therefore, Maulik et al.[30] devised a predictive framework based on local conditional probabilities for turbulence models and proposed a hybrid intelligent implicit LES approach. Their results indicated that the proposed approach exhibits robust and stable closure.

Xiao et al.[31] showed that the mean flow characteristics can largely explain the discrepancies between the results for Reynolds stress from RANS modeling and those from DNS. That study indicated that the considering uncertainty in machine learning methods is an attractive approach. Wang, Wu, and Xiao[14] established a supervised model based on random forests for discrepancies in RANS-simulated Reynolds stress tensors. Their results showed that this approach significantly improved the prediction capability for Reynolds stress compared with the original RANS simulation, but a similar improvement was not obtained in simulations of the mean velocity field. Using a SGS stress model of LES, Gamahara and Hattori[26] obtained results similar to those of Wang, Wu, and Xiao,[14] who tested ANNs as a tool for finding a new subgrid model of the SGS stress in LES. These neural network models gave better predictions of SGS stresses than the Smagorinsky model for turbulent channel flows, but their mean velocity predictions were less satisfactory. It is mainly because the mean velocity field is very sensitive to errors in Reynolds stress prediction. In order to improve the prediction of the mean velocity field, Wu, Xiao, and Paterson[32] proposed a physics-based implicit processing method to train the linear and nonlinear parts of the Reynolds stress by using machine learning and obtained satisfactory prediction accuracy of the eddy-viscosity. Wu et al.[33] derived a local condition number function as a measure to evaluate the conditional characteristics of the turbulence model, that is, to measure the sensitivity of the mean velocity at a given position of perturbation on the Reynolds stress field. It is proved that the local condition number can quantitatively explain the improvement of implicit treatment of Reynolds stress and the results in the study of Wu, Xiao, and Paterson.[32]

The aforementioned studies all aim to accurately predict the velocity field by the typical data-driven Reynolds stress model, and the Reynolds stress is obtained from a trained machine learning model without solving partial differential equations. However, most of their results are still not ideal due to the explicit treatment of Reynolds stress. Hence, it is urgent and important to construct an applicable, efficient, and accurate model, which can serve as a commonly usable tool for the industry. Based on the generalized form of Pope,[24] the present paper constructs a model using the discrepancies in Reynolds stress anisotropy between the target results of LES and the baseline results of RANS simulation. This discrepancy model is then used to train a neural network model. In addition, the trained model parameters are embedded in a computational fluid dynamics (CFD) solver by a semi-implicit treatment to modify the original RANS model aiming to improve the prediction accuracy. Finally, to explore the generalization ability and robustness of the modified model, interpolation and extrapolation modifications are performed based on the Reynolds number and two massive separation flows are also applied to modification computation.

The remainder of the paper is organized as follows. Section II derives the Reynolds stress anisotropy discrepancy model and introduces the methodology of turbulence model modification. Section III describes the numerical simulation method for training datasets and validation. Section IV presents the prediction results of the modified model and an analysis of the results. Section V discusses the main findings and concludes the paper.

II. METHODOLOGY

A. RANS turbulent-viscosity model

In this study, we employ the three-dimensional (3D) incompressible Navier–Stokes equations (NSEs) as

$$\frac{\partial u_i}{\partial x_i} = 0, \tag{1}$$

$$\frac{\partial u_i}{\partial t} + \left(u_j \frac{\partial u_i}{\partial x_j}\right) = -\frac{1}{\rho}\frac{\partial p}{\partial x_i} + \nu \frac{\partial^2 u_i}{\partial x_j^2} + f_i, \tag{2}$$

where u_i is the ith component of instantaneous velocity, p is the pressure, ρ is the density (which is constant in incompressible flows), and ν is the viscosity coefficient.

The incompressible RANS equations are obtained by taking the average of the NSEs over time, which in their form without body forces are written as

$$\frac{\partial \overline{u}_i}{\partial x_i} = 0, \tag{3}$$

$$\frac{\partial \overline{u}_i}{\partial t} + \overline{u}_j \frac{\partial \overline{u}_i}{\partial x_j} = \frac{\partial}{\partial x_j}\left(-\frac{\overline{p}}{\rho}\delta_{ij} + \nu \frac{\partial \overline{u}_i}{\partial x_j} - \overline{u_i' u_j'}\right). \tag{4}$$

Although the equations are similar to the Navier–Stokes equations, there is an additional term $(\overline{u_i' u_j'})$, which is called the Reynolds stress. The Reynolds stress is a symmetric tensor, which can be decomposed into isotropic and anisotropic parts. The decomposition results are as follows:

$$\overline{u_i' u_j'} = \frac{2}{3}\delta_{ij}k + a_{ij}, \tag{5}$$

where a_{ij} is the Reynolds stress anisotropy tensor, k is the turbulent kinetic energy, and δ_{ij} is the Kronecker delta. Therefore, a closure model is required for the anisotropy tensor. k–ε and k–ω[3,34] are the most widely used eddy-viscosity models. These models assume a linear relationship between the anisotropy tensor a_{ij} and the mean strain rate tensor $\overline{S}_{ij}$,

$$a_{ij} = -2\nu_t \overline{S}_{ij}, \tag{6}$$

where ν_t is the eddy-viscosity and $\overline{S}_{ij} = 1/2(\partial \overline{u}_i/\partial x_j + \partial \overline{u}_j/\partial x_i)$.

The standard k–ε modeled transport equations are

$$\begin{cases} \dfrac{\partial k}{\partial t} + \overline{u}_j \dfrac{\partial k}{\partial x_j} = \dfrac{\partial}{\partial x_j}\left(\dfrac{\nu_t}{\sigma_k}\dfrac{\partial k}{\partial x_j}\right) + \mathscr{P} - \varepsilon, \\[2mm] \dfrac{\partial \varepsilon}{\partial t} + \overline{u}_j \dfrac{\partial \varepsilon}{\partial x_j} = \dfrac{\partial}{\partial x_j}\left(\dfrac{\nu_t}{\sigma_\varepsilon}\dfrac{\partial \varepsilon}{\partial x_j}\right) + C_{\varepsilon 1}\dfrac{\mathscr{P}\varepsilon}{k} - C_{\varepsilon 2}\dfrac{\varepsilon^2}{k}, \end{cases} \tag{7}$$

where $\mathscr{P}$ is the production term, given by

$$\mathscr{P} = -\overline{u_i' u_j'}\frac{\partial \overline{u}_i}{\partial x_j}, \tag{8}$$

σ_k and σ_ε are set to 1.0 and 1.3, respectively, according to empirical data, and $C_{\varepsilon 1}$ and $C_{\varepsilon 2}$ are two coefficients that need to be calibrated using empirical data.

The eddy-viscosity coefficient ν_t can be calculated from $\nu_t = C_\mu k^2/\varepsilon$ by solving the above transport equation, where C_μ is set to 0.09 by the empirical relationship.

B. Turbulence model modification

The linear turbulence-viscosity model is based on the assumption of simple shear flow. For complex flows, it is possible to create higher-order turbulent-viscosity models. Pope[24] presented a general expression of a higher order turbulent-viscosity model is a function of $\hat{S}_{ij}$ and $\hat{R}_{ij}$, that is, $a_{ij} = f(\hat{S}_{ij}, \hat{R}_{ij})$, where $\hat{S}_{ij} = \overline{S}_{ij}k/\varepsilon$

$= k/(2\varepsilon)(\partial \overline{u}_i/\partial x_j + \partial \overline{u}_j/\partial x_i)$ is the normalized mean strain rate tensor and $\hat{R}_{ij} = \overline{R}_{ij}k/\varepsilon = k/(2\varepsilon)(\partial \overline{u}_i/\partial x_j - \partial \overline{u}_j/\partial x_i)$ is the normalized mean rotation rate tensor. Eventually, a_{ij} can be expressed as a linear combination of ten isotropic basis tensors in 3D incompressible flow,

$$a_{ij} = k\sum_{n=1}^{10} G^n(\lambda_1, \lambda_2, \lambda_3, \lambda_4, \lambda_5) T_{ij}^n. \tag{9}$$

The basis tensors $\mathbf{T}$ are given by

$$\begin{aligned}
\mathbf{T}^1 &= \hat{\mathbf{S}}, \\
\mathbf{T}^2 &= \hat{\mathbf{S}}\hat{\mathbf{R}} - \hat{\mathbf{R}}\hat{\mathbf{S}}, \\
\mathbf{T}^3 &= \hat{\mathbf{S}}^2 - \frac{1}{3}\mathbf{I}_3 \cdot Tr(\hat{\mathbf{S}}^2), \\
\mathbf{T}^4 &= \hat{\mathbf{R}}^2 - \frac{1}{3}\mathbf{I}_3 \cdot Tr(\hat{\mathbf{R}}^2), \\
\mathbf{T}^5 &= \hat{\mathbf{R}}\hat{\mathbf{S}}^2 - \hat{\mathbf{S}}^2\hat{\mathbf{R}}, \\
\mathbf{T}^6 &= \hat{\mathbf{R}}^2\hat{\mathbf{S}} + \hat{\mathbf{S}}\hat{\mathbf{R}}^2 - \frac{2}{3}\mathbf{I}_3 \cdot Tr(\hat{\mathbf{S}}\hat{\mathbf{R}}^2), \\
\mathbf{T}^7 &= \hat{\mathbf{R}}\hat{\mathbf{S}}\hat{\mathbf{R}}^2 - \hat{\mathbf{R}}^2\hat{\mathbf{S}}\hat{\mathbf{R}}, \\
\mathbf{T}^8 &= \hat{\mathbf{S}}\hat{\mathbf{R}}\hat{\mathbf{S}}^2 - \hat{\mathbf{S}}^2\hat{\mathbf{R}}\hat{\mathbf{S}}, \\
\mathbf{T}^9 &= \hat{\mathbf{R}}^2\hat{\mathbf{S}}^2 + \hat{\mathbf{S}}^2\hat{\mathbf{R}}^2 - \frac{2}{3}\mathbf{I}_3 \cdot Tr(\hat{\mathbf{S}}^2\hat{\mathbf{R}}^2), \\
\mathbf{T}^{10} &= \hat{\mathbf{R}}\hat{\mathbf{S}}^2\hat{\mathbf{R}}^2 - \hat{\mathbf{R}}^2\hat{\mathbf{S}}^2\hat{\mathbf{R}},
\end{aligned} \tag{10}$$

and invariants λ are given by

$$\begin{aligned}
\lambda_1 &= Tr(\hat{\mathbf{S}}^2), \quad \lambda_2 = Tr(\hat{\mathbf{R}}^2), \quad \lambda_3 = Tr(\hat{\mathbf{S}}^3), \\
\lambda_4 &= Tr(\hat{\mathbf{R}}^2\hat{\mathbf{S}}), \quad \lambda_5 = Tr(\hat{\mathbf{R}}^2\hat{\mathbf{S}}^2).
\end{aligned} \tag{11}$$

For flows that are statistically two-dimensional, the situation is considerably simpler. The tensors $\mathbf{T}^1$, $\mathbf{T}^2$, and $\mathbf{T}^3$ form an integrity basis, and invariants λ are given by

$$\lambda_1 = Tr(\hat{\mathbf{S}}^2), \quad \lambda_2 = Tr(\hat{\mathbf{R}}^2). \tag{12}$$

Furthermore, the term in $\mathbf{T}^3$ can be absorbed into the modified pressure so that $G^3 = 0$. Therefore, the higher-order turbulent-viscosity model for statistically two-dimensional flows is[35]

$$a_{ij} = k(G^1 T_{ij}^1 + G^2 T_{ij}^2). \tag{13}$$

Taking into account the periodic boundary conditions and the two-dimensional characteristics of the geometry of the periodic hill flow, and constructing a more universal model, the constitutive equation we are trying to train in this study only requires four basis tensors,[35,36]

$$a_{ij} = k(G^1 T_{ij}^1 + G^2 T_{ij}^2 + G^3 T_{ij}^3 + G^4 T_{ij}^4). \tag{14}$$

Therefore, the discrepancies between the anisotropy tensors obtained by the higher-order turbulent-viscosity model (a_{ij}) and

the traditional turbulent-viscosity model $(-2\nu_t \overline{S}_{ij})$ are

$$\Delta a_{ij} = a_{ij} - (-2\nu_t \overline{S}_{ij})$$

$$= k \sum_{n=0}^{2} G^n(\lambda_1, \lambda_2) T_{ij}^n - (-2\nu_t \overline{S}_{ij})$$

$$= k G^0 T_{ij}^0 + k G^1 \hat{S}_{ij} + k G^2 T_{ij}^2 + 2\nu_t \frac{\varepsilon}{k} \hat{S}_{ij}$$

$$= k G^0 T_{ij}^0 + k\left(G^1 + \frac{2\nu_t \varepsilon}{k^2}\right)\hat{S}_{ij} + k G^2 T_{ij}^2. \qquad (15)$$

Then,

$$\Delta a_{ij} = k G^0 T_{ij}^0 + k\left(G^1 + \frac{2\nu_t \varepsilon}{k^2}\right)T_{ij}^1 + k G^2 T_{ij}^2. \qquad (16)$$

Obviously, the discrepancies in the anisotropy tensors can also be expressed as the generalized form of Pope.[24]

In order to improve the performance of the original RANS model in capturing the anisotropy of the flow field, a semi-implicit discrepancy model is constructed. A fully connected neural network is trained based on the above discrepancy model. Figure 1 presents a flow diagram of a supervised learning algorithm applied in the RANS turbulence model. The LES method is performed to generate target data a_{ij}^{LES}, and the RANS k–ε model is used to obtain the baseline data a_{ij}^{RANS}. The 3D LES data are spanwise averaged and then linearly interpolated to correspond to the simulated 2D RANS data under the coarse grid. The discrepancies $\Delta a_{ij} = a_{ij}^{LES} - a_{ij}^{RANS}$ are computed as the output of the neural network, and the regression function $f : \mathbf{q} \to \Delta a_{ij}$ is constructed, where $\mathbf{q} = \{\lambda_1, \lambda_2\}$ is chosen as the input features.

The trained regression function f is used to predict the anisotropy discrepancy tensors Δa_{ij} for the modified flow, and the modified anisotropy tensors a_{ij} are obtained by adding the predicted discrepancy tensors Δa_{ij} to the anisotropy tensors a_{ij}^{RANS} simulated

by the original RANS model,

$$a_{ij} = \Delta a_{ij} + a_{ij}^{RANS} = \Delta a_{ij} - 2\nu_t \overline{S}_{ij}. \qquad (17)$$

Then, the modified Reynolds stress tensors are also obtained by adding the modified anisotropic tensors a_{ij} to the isotropic tensors $\frac{2}{3}\delta_{ij}k$,

$$\overline{u_i' u_j'} = a_{ij} + \frac{2}{3}\delta_{ij}k = \Delta a_{ij} - 2\nu_t \overline{S}_{ij} + \frac{2}{3}\delta_{ij}k. \qquad (18)$$

Therefore, the modified RANS equation can be expressed as

$$\frac{\partial \bar{u}_i}{\partial t} + \bar{u}_j \frac{\partial \bar{u}_i}{\partial x_j}$$

$$= \frac{\partial}{\partial x_j}\left[-\frac{\bar{p}}{\rho}\delta_{ij} + \nu \frac{\partial \bar{u}_i}{\partial x_j} - \left(\underbrace{\Delta a_{ij}}_{explicit} \underbrace{-2\nu_t \overline{S}_{ij} + \frac{2}{3}\delta_{ij}k}_{implicit}\right)\right]. \qquad (19)$$

It can be seen that Eq. (19) has no diffusion flux for implicitly discretizing. However, the discretization of equations based on the finite volume method (FVM) generates a numerical diffusion.[37] Therefore, the modified Reynolds stress in Eq. (19) is decomposed into two terms for numerical considerations.[38] The linear part of the Reynolds stress is treated implicitly by the original RANS model, while the non-linear part is explicitly predicted by the neural network.

Compared with the original RANS equation, the source terms added in the modified momentum equation are

$$S_{u1} = -\left(\frac{\partial \Delta a_{11}}{\partial x} + \frac{\partial \Delta a_{12}}{\partial y}\right),$$

$$S_{u2} = -\left(\frac{\partial \Delta a_{12}}{\partial x} + \frac{\partial \Delta a_{22}}{\partial y}\right).$$
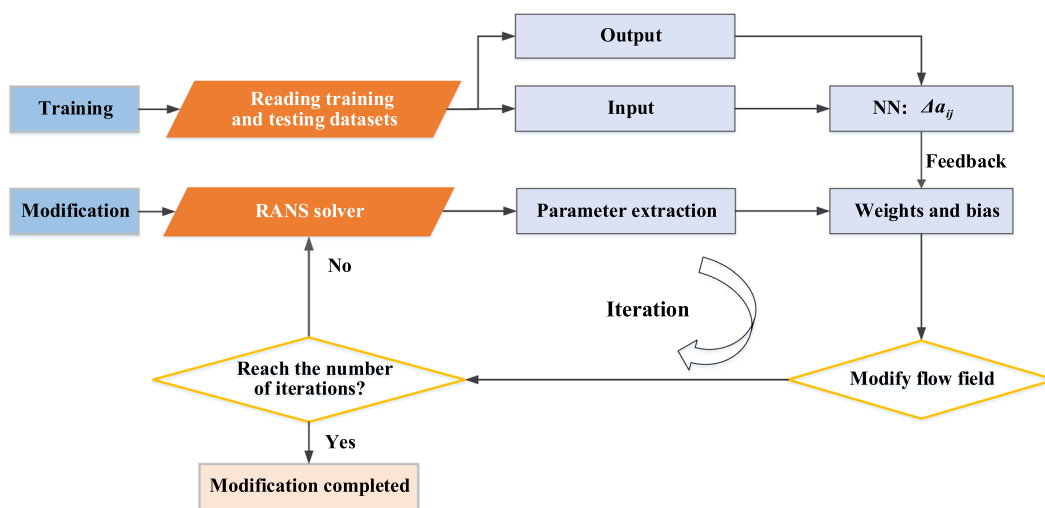

FIG. 1. Framework for modification of the turbulence model.

The corresponding time-discrete momentum equation is as follows:

$$\frac{\bar{u}_i^{n+1} - \bar{u}_i^n}{\Delta t} + \bar{u}_j^n \frac{\partial \bar{u}_i^{n+1}}{\partial x_j} = -\frac{1}{\rho}\left(\frac{\partial \bar{p}}{\partial x_i}\right)^{n+1} + \frac{\partial}{\partial x_j}\left(\nu \frac{\partial \bar{u}_i^{n+1}}{\partial x_j}\right)$$

$$- \frac{\partial}{\partial x_j}\left(\Delta a_{ij}^{*n} - \nu_t \frac{\partial \bar{u}_i^{n+1}}{\partial x_j} - \nu_t \frac{\partial \bar{u}_j^{n+1}}{\partial x_i} + \frac{2}{3}\delta_{ij}k^n\right), \quad (20)$$

where the superscript indicates the calculation result of the nth time step or the $(n + 1)$th time step. Equation (20) gives the velocity prediction of the fluid, which is corrected by the updated pressure at the $(n + 1)$th time step.

The modified transport equations for the turbulent kinetic energy k and dissipation rate ε are

$$\frac{\partial k}{\partial t} + \bar{u}_j \frac{\partial k}{\partial x_j} = \frac{\partial}{\partial x_j}\left(\frac{\nu_t}{\sigma_k}\frac{\partial k}{\partial x_j}\right) + (\mathscr{P} + \mathscr{P}^*) - \varepsilon, \quad (21)$$

$$\frac{\partial \varepsilon}{\partial t} + \bar{u}_j \frac{\partial \varepsilon}{\partial x_j} = \frac{\partial}{\partial x_j}\left(\frac{\nu_t}{\sigma_\varepsilon}\frac{\partial \varepsilon}{\partial x_j}\right) + C_{\varepsilon 1}\frac{(\mathscr{P} + \mathscr{P}^*)\varepsilon}{k} - C_{\varepsilon 2}\frac{\varepsilon^2}{k}, \quad (22)$$

where $\mathscr{P}^*$ is the modification of production term, given by

$$\mathscr{P}^* = -\Delta a_{ij}^* \frac{\partial \bar{u}_i}{\partial x_j}. \quad (23)$$

Therefore, the source terms added in the two modified transport equations are

$$S_k = \mathscr{P}^*, \qquad S_\varepsilon = C_{\varepsilon 1}\frac{\mathscr{P}^* \varepsilon}{k}.$$

In this semi-implicit modification computation, a relaxation coefficient γ is used to ensure that the computation does not fail to converge owing to an excessive source term. The value of γ gradually changes from 0 to 1 as the iteration step increases. Therefore, the final modified source terms S_{u1_γ} and S_{u2_γ} in the momentum equation and the modified source terms S_{k_γ} and S_{ε_γ} in the transport equation are

$$\begin{cases} S_{u1\_\gamma} = -\gamma\left(\dfrac{\partial \Delta a_{11}}{\partial x} + \dfrac{\partial \Delta a_{12}}{\partial y}\right), \\ S_{u2\_\gamma} = -\gamma\left(\dfrac{\partial \Delta a_{12}}{\partial x} + \dfrac{\partial \Delta a_{22}}{\partial y}\right), \\ S_{k\_\gamma} = \gamma\mathscr{P}^*, \\ S_{\varepsilon\_\gamma} = C_{\varepsilon 1}\dfrac{\gamma\mathscr{P}^* \varepsilon}{k}. \end{cases} \quad (24)$$

C. Neural network structure and parameters

In this approach, a fully connected deep neural network (DNN) is employed to establish a functional relationship between the mean flow field and the Reynolds stress anisotropy discrepancy. Figure 2 is a schematic of the DNN. The DNN consists of an input layer, the hidden layers, and an output layer. Neurons in any layer receive a set of inputs from the previous layer, and they then output a set of data. That is, each neuron in layer l is connected to all neurons in layer $l - 1$ (this is the meaning of fully connected), and the output $a_j(l - 1)$ of neurons in layer $l - 1$ is the input of neurons in layer l. Each connection between the two layers has a weight W, which is the model parameter that the neural network needs to learn. Take the ith neuron node of the lth layer as an example, the value of this neuron is

$$z_i(l) = \sum_{j=1}^{n} W_{ij}(l)a_j(l - 1) + b_i(l) \quad (25)$$

and $z_i(l)$ is applied to the activation function to get the output result $a_i(l)$ of this neuron,

$$a_i(l) = \sigma[z_i(l)], \quad (26)$$

where $b_i(l)$ is the bias and f is the activation function. The activation function σ in this network is the leaky rectified linear unit (leaky ReLU)[39] and is expressed as

$$\sigma(x) = \begin{cases} \alpha x, & x < 0 \\ x, & x \geq 0, \end{cases} \quad (27)$$

In this paper, the RANS model is used for baseline computation and the results of LES are used as the target results. The output parameter of neural network are the discrepancies
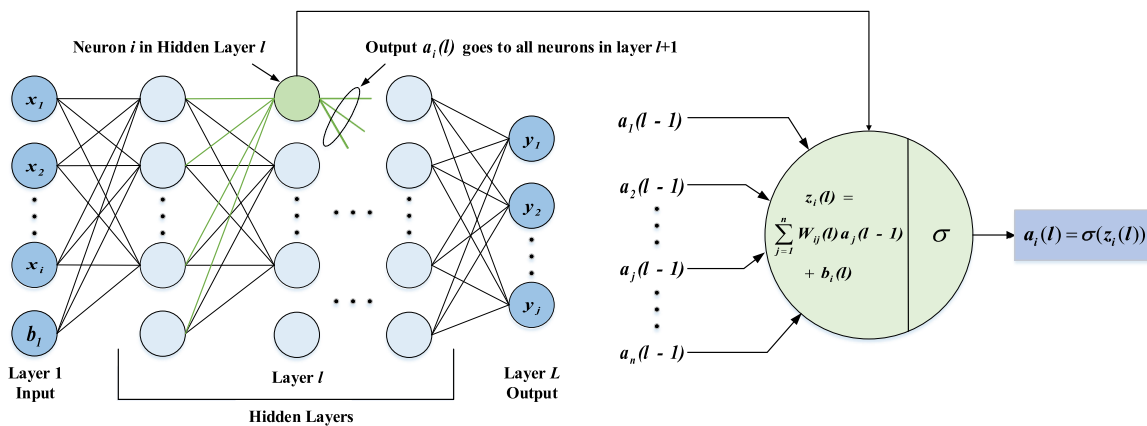

FIG. 2. Schematic diagram of the DNN.

TABLE I. Cases used for discrepancy model training and the original RANS model modification.

Cases	Discrepancy model training cases	Modification cases
P1	Re = 2800, 8400, 10 595	Re = 5 600
P2	Re = 2800, 5600, 8400	Re = 10 595

Δa_{ij} in the Reynolds stress anisotropy between the target result a_{ij}^{LES} and the baseline result a_{ij}^{RANS}. The input parameters are $\lambda_1 = Tr(\hat{\mathbf{S}}^2) = Tr(\overline{S}_{ij}\overline{S}_{ij}k^2/\varepsilon^2)$ and $\lambda_2 = Tr(\hat{\mathbf{R}}^2) = Tr(\overline{R}_{ij}\overline{R}_{ij}k^2/\varepsilon^2)$, which are the invariants. The mean strain rate tensor $\overline{S}_{ij}$ and the mean rotation rate tensor $\overline{R}_{ij}$ are both obtained by the LES results and are non-dimensionlized by the turbulent kinetic energy k and dissipation rate ε in the RANS results, which adds effective information of RANS to the neural network. The hidden layer is set to 4 layers, each with 20 neuron nodes. The datasets that we use for model training is provided in Table I. α in the activation function is taken as 10^{-8}.

To minimize the error between the output and the given Reynolds stress anisotropy discrepancy Δa_{ij}, gradient descent backpropagation is used to iterate the weights and optimize the bias parameters. The loss function is given by

$$\sqrt{\frac{1}{4N}\sum_{m=1}^{N}\left[\sum_{i=1}^{3}\sum_{j=1}^{i}\left(\Delta a_{ij} - \Delta a_{ij}^{NN}\right)\left(\Delta a_{ij} - \Delta a_{ij}^{NN}\right)\right]}$$
$$+ \alpha'\|\mathbf{W}\|_2^2, \tag{28}$$

where Δa_{ij}^{NN} is the output of the network, M indicates the number of the current set, α' is the regularization coefficient, which is given as 0.0005, and $\|\mathbf{W}\|_2^2$ is the regularization term, which is used to prevent overfitting.[40]

III. NUMERICAL SIMULATIONS

Periodic hill flow has typical characteristics of flow separation, recirculation, and reattachment.[41] Separation induced by pressure occurs from the curved surface, and reattachment is observed on the plate. These flow characteristics of periodic hill flow are therefore sensitive to various features of flow modeling and numerical simulations. Periodic hill flow is widely used as a test case to study the ability of the RANS model and LES approach in the curved geometry to model flow separation and simulate physical mechanisms.

A. Governing equations

Periodic hill flow has been extensively studied because of its periodic boundary conditions and symmetrical geometry. Peller and Manhart[42] performed DNS of periodic hill flow up to a Reynolds number of Re = $U_B h/\nu$ = 5600 (based on the bulk velocity U_B, hill crest h, and kinematic viscosity coefficient ν). Fröhlich et al.,[43] Breuer et al.,[41] and Temmerman and Leschziner[44] performed LES of separated periodic hill flow at Re = 10 595. To overcome the limitation of these previous studies to high Reynolds numbers, the present paper explores the prediction capability of deep learning models over a wide range of Reynolds numbers by using LES to perform numerical simulations of periodic hill flow.

To study the characteristics of the periodic hill flow, a filter function $G(\mathbf{x}, \boldsymbol{\xi}; \Delta)$ is used to obtain the filtered physical variable such as $\widetilde{u}(\mathbf{x}, t) = \int G(\mathbf{x}, \boldsymbol{\xi}; \Delta)\mathbf{u}(\boldsymbol{\xi}, t)d\boldsymbol{\xi}$. $\Delta = \sqrt[3]{\Delta x \Delta y \Delta z}$ is the spatial filter scale determined using an explicit box filter, where Δ is the side length of the grid cell under the Cartesian grid. The filtered momentum equation can be deduced by making operation on the above momentum equation as

$$\frac{\partial \widetilde{u}_i}{\partial x_i} = 0, \tag{29}$$

$$\frac{\partial \widetilde{u}_i}{\partial t} + \left(\widetilde{u}_j\frac{\partial \widetilde{u}_i}{\partial x_j}\right) = -\frac{1}{\rho}\frac{\partial \widetilde{p}}{\partial x_i} + \frac{\partial(2\nu\widetilde{S}_{ij})}{\partial x_j} - \frac{\partial \tau_{ij}}{\partial x_j} + \widetilde{f}_i, \tag{30}$$

where $\widetilde{u}_i$ is the filtered ith velocity component, $\widetilde{p}$ is the filtered pressure, $\widetilde{S}_{ij} = 1/2(\partial \widetilde{u}_i/\partial x_j + \partial \widetilde{u}_j/\partial x_i)$ is the filtered strain-rate tensor, and the term $\tau_{ij} = \widetilde{u_i u_j} - \widetilde{u}_i\widetilde{u}_j$ is the subgrid-scale (SGS) stress, which results from the unresolved subgrid-scale and needs to be modeled by an SGS model. The flow in this study is driven by a mean velocity force so as to yield the global mass flux.

B. Subgrid-scale modeling

The sub-lattice quantities are unknown, so it is necessary to establish corresponding models for them. The SGS stress in this paper is modeled by the One-equation eddy-viscosity model (OEM) (Yoshizawa[45]). Compared with the Smagorinsky model, this model has a more accurate time scale. The one-equation eddy-viscosity SGS model uses the eddy-viscosity approximation, so the anisotropic part of the SGS stress tensor is modeled as

$$\tau_{ij} - \frac{1}{3}\delta_{ij}\tau_{kk} = -2\nu_{SGS}\widetilde{S}_{ij}, \tag{31}$$

where the trace τ_{kk} is lumped into a modified pressure and does not need to be considered. ν_t is the SGS viscosity and is computed using k_{SGS} as $\nu_{SGS} = C_k\Delta\sqrt{k_{SGS}}$, A transportation equation is derived to account for the historic effect of k_{SGS} due to production, dissipation, and diffusion,

$$\frac{\partial k_{SGS}}{\partial t} + \widetilde{u}_j\frac{\partial(k_{SGS})}{\partial x_j} - \frac{\partial}{\partial x_j}\left[(\nu + \nu_{SGS})\frac{\partial(k_{SGS})}{\partial x_j}\right]$$
$$= 2\nu_{SGS}\frac{\partial \widetilde{u}_i}{\partial x_j}\widetilde{S}_{ij} - C_\varepsilon\frac{k_{SGS}^{3/2}}{\Delta}, \tag{32}$$

where C_k is the model constant whose default value is 0.094 and C_ε is another model constant whose default value is 1.048.

C. Numerical scheme

Figure 3 illustrates the geometry adopted in the simulations. The dimensions of the computation are the hill-crest separation L_x, the channel height L_y, and the span length L_z, which are set to 9.0h, 3.035h, and 4.5h, respectively. The computational domain contains $N_x \times N_y \times N_z$ = 200 × 160 × 80 interior cells, and periodic boundary conditions are carried out. Near the lower wall, no-slip conditions are applied. In addition, the near-wall processing method is wall-resolved LES. This is because y^+ corresponding to the height of the first layer of grid is less than 1.

In the present study, five simulation datasets, each for different Reynolds numbers Re = 2800, 5600, 8400, and 10 595, are obtained
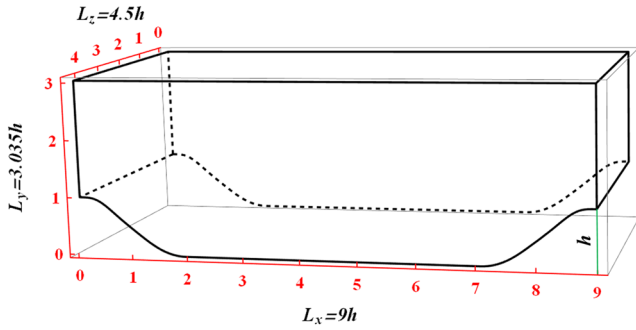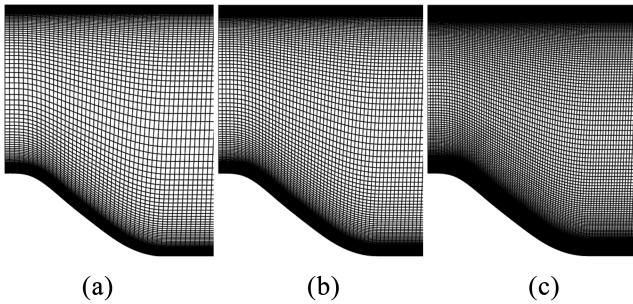
FIG. 3. Geometry of the periodic hill flow.

FIG. 4. Three mesh sizes for LES simulation. (a) Coarse mesh, (b) original mesh, and (c) fine mesh.
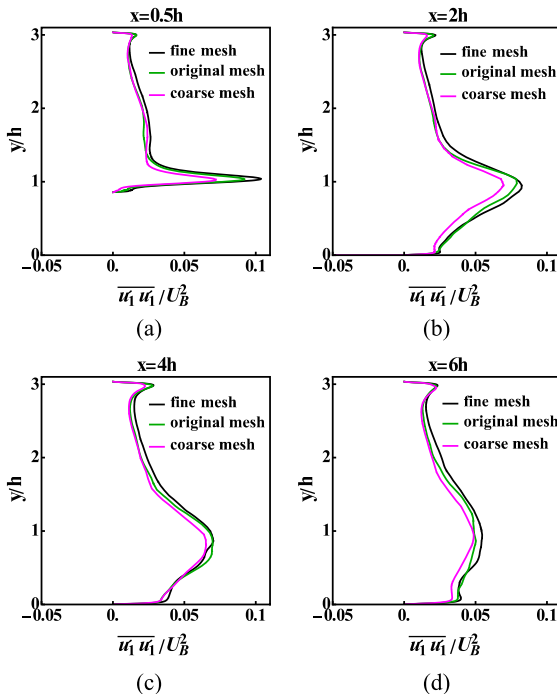
by performing LES of periodic hill flow. Besides the original mesh, a new coarse mesh and a fine mesh are presented in Fig. 4. The computational domain of coarse and fine meshes contains $N_x \times N_y \times N_z$ = 141 × 113 × 57 and $N_x \times N_y \times N_z$ = 283 × 226 × 113 interior cells, respectively.

The LES database provides the averaged second-order correlation fields of the fluctuating velocity, which is the Reynolds stress field on the LES grids according to the definition. The results of normal stress components ($\overline{u_1' u_1'}$) and shear stress components ($\overline{u_1' u_2'}$) for three mesh sizes at Re = 10 595 are shown in Figs. 5 and 6, respectively. Figures 5 and 6 show that the results simulated by the original mesh and fine mesh agree well with each other in both trend and magnitude, which verify the validity of the present mesh size.

Figure 7 displays an instantaneous characteristic of the flow field, namely, the streamline velocity. It can be seen that there are a few typical regions of the periodic hill flow. First, on the left curved surface, flow separation begins to occur owing to the reverse pressure gradient, and a recirculation zone is then formed along the streamline direction. Finally, with the geometric contraction and the accompanying pressure gradient, the flow reattaches before it reaches the next hill crest with the formation of a recovery region. The flow characteristics of these typical regions will be the main concerns of the validation in Sec. III D and the analysis of results in Sec. IV.
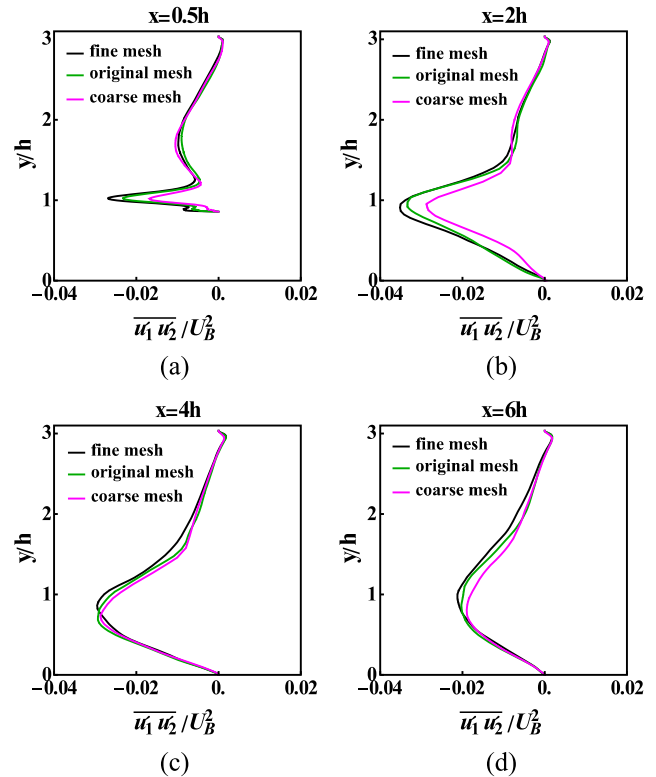

FIG. 5. Results of normal stress components ($\overline{u_1' u_1'}$) of the LES approach for three mesh sizes. (a) x/h = 0.5, (b) x/h = 2, (c) x/h = 4, and (d) x/h = 6.

FIG. 6. Results of normal stress components ($\overline{u_1' u_2'}$) of the LES approach for three mesh sizes. (a) x/h = 0.5, (b) x/h = 2, (c) x/h = 4, and (d) x/h = 6.
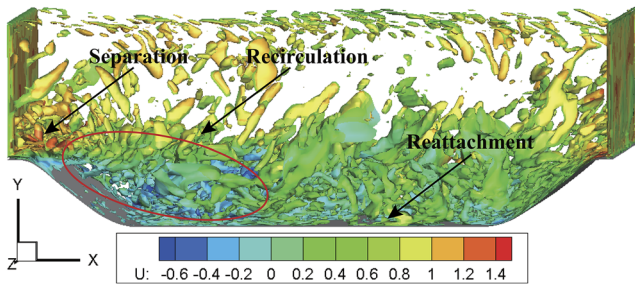
FIG. 7. Instantaneous streamline velocity based on the Q criterion.

D. Validation of simulation results

Figure 8 presents the mean streamline velocity and second-order fluctuation statistics of the periodic hill flow as computed by LES and by RANS. For comparison, it also shows the experimental results of Rapp, Pfleger, and Manhart[46] and the DNS results of Breuer et al.[41] According to the experimental results,[46] the flow begins to separate at $x/h = 0.5$, $x/h = 2$ is the center of the flow recirculation region, $x/h = 4$ is the position of the reattachment point, and $x/h = 6$ is the position of flow recovery [see Fig. 8(a)]. It can be seen from the mean velocity profile in Fig. 8(a) that the results of LES are closely consistent with the experimental/DNS results. Meanwhile, the normal stress components [Figs. 8(b) and 8(d)] and the shear stress components [Fig. 8(c)] are also consistent with the experimental/DNS results. Therefore, this comparison indicates that the datasets computed using LES can be used to train the neural network that will be used to modify the RANS turbulence model.

IV. RESULTS AND DISCUSSION

The cases used for neural network model training and modification are provided in Table I, where P stands for two periodic hill cases, with $P1$ and $P2$ being the modification results for Re = 5600 and 10 595, respectively. The modification flow field is a new case computed by Fluent, which does not participate in the neural network model training. In the previous study of turbulence modeling by machine learning methods, the research results presented that the prediction accuracy for the Reynolds stress was improved, but no significant improvement was observed for the mean velocity field. In the present paper, therefore, the prediction accuracy of the Reynolds stress using the modified model was computed for two cases compared to the results of LES and RANS, and then the velocity profiles were also compared. Finally, one of two cases was used as an example to study the prediction accuracy of the mean pressure coefficient and the mean friction coefficient on the underlying wall surface.

In order to explore the predictive performance of the modified model, the previously trained model is also directly performed for the modification computation of the two massive separation periodic hill flows in Sec. IV D.

A. Prediction of Reynolds stress anisotropy

The Reynolds stress anisotropy tensor a_{ij} is symmetric, and its eigenvalues are real.[47] It can be therefore defined through the following similarity transformation:
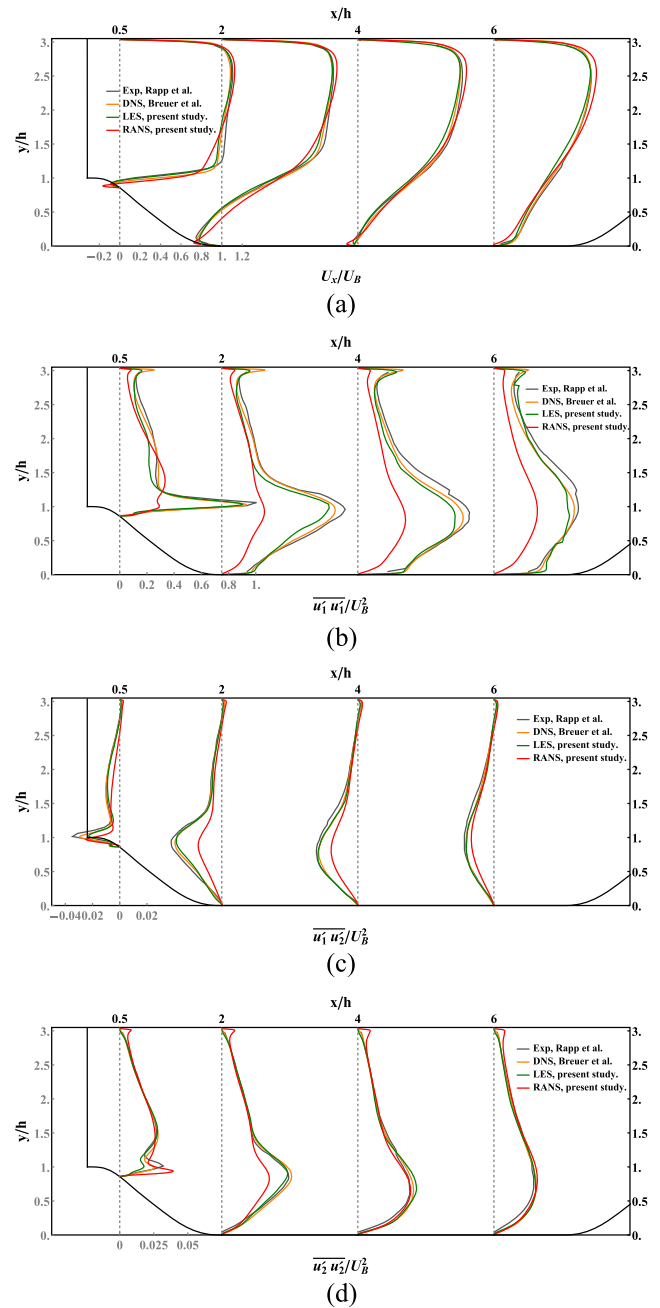

FIG. 8. Results from LES and RANS, compared with the experimental results of Rapp, Pfleger, and Manhart[46] and the DNS results of Breuer et al.[41] for the profiles of (a) mean streamline velocity U_x/U_B, (b) normal stress components $\overline{u_1' u_1'}/U_B^2$, (c) shear stress components $\overline{u_1' u_2'}/U_B^2$, and (d) normal stress components $\overline{u_2' u_2'}/U_B^2$ at four different locations ($x/h = 0.5, 2, 4, 6$).

$$X_{ik} a_{kn} X_{nj} = 2k(\lambda^i \delta_{ij}), \tag{33}$$

where X_{ij} is the matrix containing the eigenvectors of $a_{ij}/2k$ and $\lambda^i \delta_{ij}$ is the diagonal matrix with the eigenvalues of $a_{ij}/2k$. The barycentric coordinates of the barycentric map are then obtained

using the eigenvalues,[47] as follows:

$$C_{1c} = \lambda^1 - \lambda^2, \quad C_{2c} = 2(\lambda^2 - \lambda^3), \quad C_{3c} = 3\lambda^3 + 1, \quad (34)$$

and $C_{1c} + C_{2c} + C_{3c} = 1$. The points (x, y) in the barycentric map can be expressed in terms of the coordinates of three vertices (x_{1c}, y_{1c}), (x_{2c}, y_{2c}), and (x_{3c}, y_{3c}),

$$x = C_{1c}x_{1c} + C_{2c}x_{2c} + C_{3c}x_{3c},$$
$$y = C_{1c}y_{1c} + C_{2c}y_{2c} + C_{3c}y_{3c}. \quad (35)$$

The plots of the turbulent states in triangles can be used to evaluate the prediction performance of the modified model. The predicted Reynolds stress anisotropy is displayed in Fig. 9 for two cases (modifications with Re = 5600 and Re = 10 595). The prediction results of the original RANS model evolve along a line termed plane strain, which is significantly different from the LES result. However, compared with the original RANS model, the ability of the modified model to capture anisotropic features has been improved. The qualitative curve direction and the topology of the graph of the modified model are consistent with the LES.

B. Prediction of the velocity

It is very difficult to predict the velocity field based on a typical data-driven Reynolds stress model under the DNN framework. This is mainly because the mean velocity field is very sensitive to errors in Reynolds stress prediction. However, the discrepancies between the Reynolds stress computed by the high-fidelity algorithm and RANS

model can better reflect the differences in the typical characteristics of the mean flow field. Therefore, this section will focus on analyzing and discussing the prediction results of the velocity profiles.

Interpolated and extrapolated modifications of the RANS turbulence model are performed based on the Reynolds number. An example of a velocity contour map is depicted in Fig. 10 for case P1 (Re = 5600). Figures 10(a)–10(c) correspond to LES, the modified model, and the RANS model, respectively.

From the velocity contours of the mean flow, it can be seen that the prediction of flow separation and reattachment by the original RANS model is not accurate enough, whereas the modified model shows an obvious improvement in this respect and is consistent with the LES results. Furthermore, the computational result in the recirculation region is consistent with the physical properties, although slight hysteresis occurs at the computed reattachment point compared with the LES results.

Furthermore, the root mean square error (RMSE) is used to quantify the deviations in the x-direction velocity between the prediction results of the modified model and the original RANS model compared with those of LES. It is given by RMSE $= \sqrt{1/n \sum (\hat{u}_i - \bar{u}_i)^2}$, where $\hat{u}_i$ is the x-direction mean velocity from LES, $\bar{u}_i$ is the prediction result of the modified model or the original RANS model, and n indicates the number of grids in a flow field. Table II shows the RMSE for cases P1 and P2. It can be seen that in each case, the RMSE values for the modified model are significantly lower than those for the original model.

In this paper, the volume flowrate is used as an indicator to further verify the prediction performance of the modified model
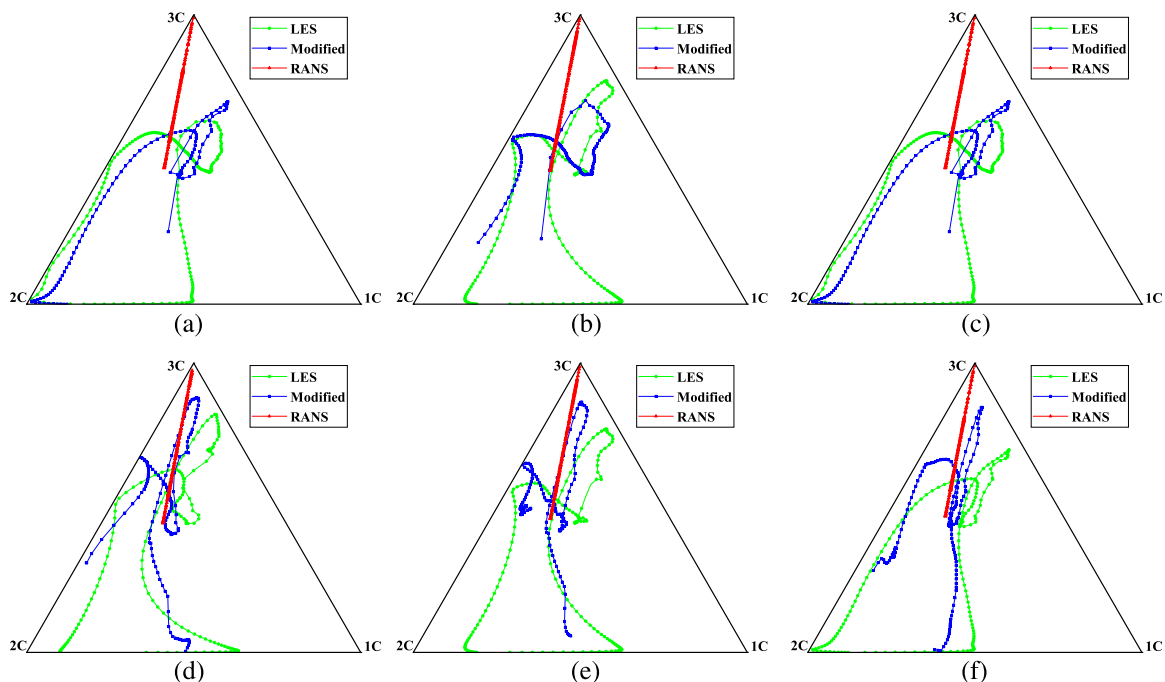

FIG. 9. Prediction performance for the Reynolds stress anisotropy for two cases (Re = 5600 and Re = 10 595) using LES, the modified model, and the original RANS model at three locations (x/h = 2, 4, 6), plotted as barycentric maps with (a) x/h = 2, Re = 5600; (b) x/h = 4, Re = 5600; (c) x/h = 6, Re = 5600; (d) x/h = 2, Re = 10 595; (e) x/h = 4, Re = 10 595; and (f) x/h = 6, Re = 10 595.
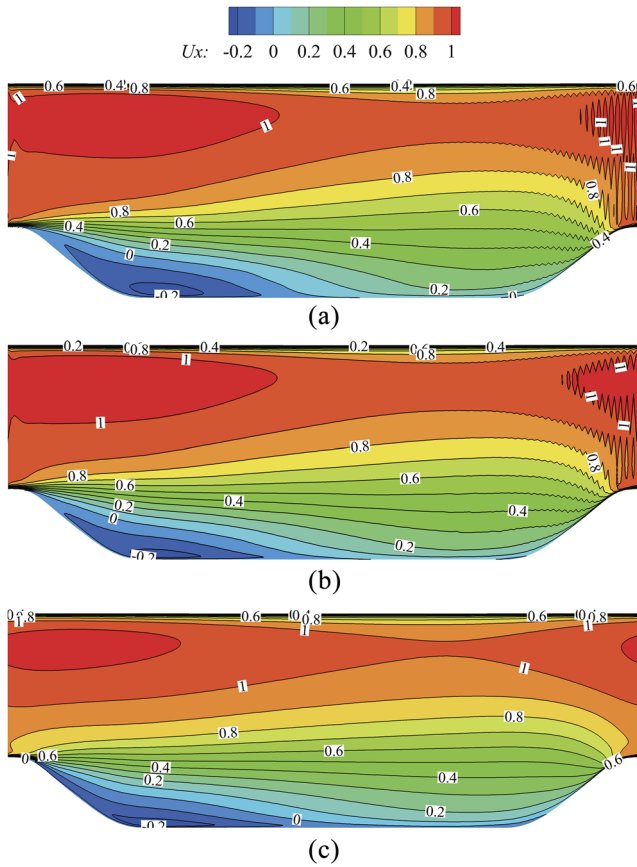
FIG. 10. Predicted velocity contour maps for the mean flow using (a) LES, (b) the modified model, and (c) the original RANS model at Re = 5600.

TABLE III. Volume flowrate for two cases obtained by LES, the modified model, and the original RANS model.

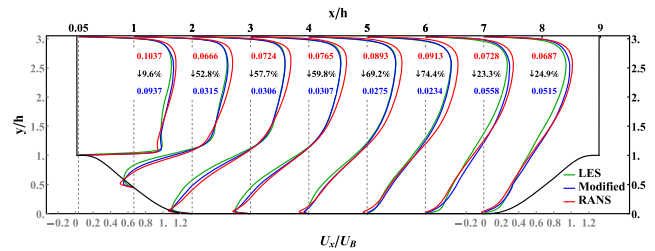| Cases	LES	Modified model	RANS model
P1: Re = 5600	0.0533	0.0554	0.0568
P2: Re = 10 595	0.0535	0.0531	0.0528

FIG. 11. Predictions of the mean x-direction velocity (U_x/U_B) profile using the modified model compared with the predictions using LES and the original RANS model at Re = 5600. The blue and red numbers are the RMSE values from the modified model and the original RANS model, respectively, and the black numbers are the deviation reduction.

from a macro perspective. The computation results of the volume flowrate listed in Table III show that the prediction results of the modified model are closer to the target results (LES) than the original RANS model because the volume flow rate is closely related to the prediction accuracy of the flow field velocity. In addition, we also specifically analyze the prediction results of the velocity profile.

Figure 11 compares the distribution of mean x-direction velocity U_x/U_B at different vertical positions in the flow field, $x/h = 0.05, 1, 2, \ldots, 7$. It can be seen that the modified model is able to give more accurate predictions of the mean velocity profile compared with the RANS model. The deviations (RMSE) of the different velocity profiles (see the blue and red numbers in Fig. 11) also confirm that the modified model outperforms the original RANS model.

The numbers in black in Fig. 11 indicate the deviation reduction of the modified model. It can be seen that the modified model alters the valley flow most significantly. The reverse flow expands to the position of $x/h = 4$ in LES results; however, the RANS model overestimates the end of the recirculation zone because the velocity field still has negative values at $x/h = 5$. Meanwhile, the RANS model also underestimates the velocity gradient near the wall area of the recirculation zone ($x/h = 1, 2, 3$). The modified model not only improves the prediction of the velocity gradient but also improves the prediction of the separation bubble size. Hence, we can conclude that, compared with the RANS model, the modified model is better at simulating fluctuations in the shear layer and in determining the location of end point of the reverse flow.

Case P2 in Table II is an extrapolation computation based on the Reynolds number, and the flow at Re = 10 595 is modified. The results of the velocity prediction for different profiles are shown in Fig. 12. It can be seen that the extrapolated modification still captures the flow characteristics more accurately than the original
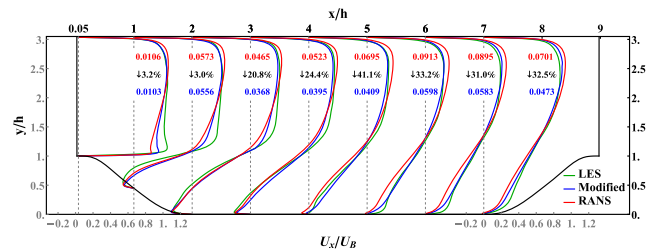
TABLE II. RMSE of velocity for two cases obtained by comparing the predicted results of the modified model and of the original RANS model with those of the LES.

Cases	Modified model	RANS model
P1: Re = 5600	0.048	0.081
P2: Re = 10 595	0.046	0.064

FIG. 12. Predictions of the mean x-direction velocity (U_x/U_B) profile using the modified model compared with the predictions using LES and the original RANS model at Re = 10 595. The blue and red numbers are the RMSE values from the modified model and the original RANS model, respectively, and the black numbers are the deviation reduction.
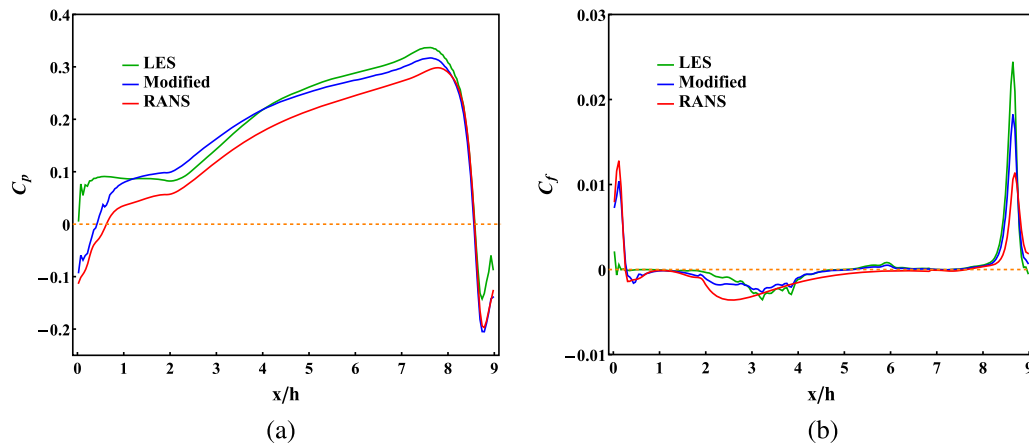
FIG. 13. Predictions of (a) the mean pressure coefficient C_p and (b) the mean friction coefficient C_f obtained using LES, the modified model, and the RANS model at Re = 5600.

RANS model, especially in the prediction for the length of recirculation zone. In addition, the deviation reduction indicated by the black numbers in Fig. 12 also further demonstrates that the prediction performance of the modified model is superior to the original RANS model.

C. Prediction of the mean pressure and friction coefficients

Periodic hill flow is a standard case for evaluating turbulent simulation in complex boundary walls. Therefore, it is appropriate to evaluate the prediction performance of the modified model using the pressure and friction coefficient predictions near the wall as indicators.

Figure 13 presents the distributions of the mean pressure coefficient C_p and the mean friction coefficient C_f on the underlying wall surface of the periodic hill. It can be seen from Fig. 13(a) that, compared with LES, the original RANS model underestimates the pressure in the valley region, and the capture of pressure peaks is significantly delayed because of the overestimation of the recirculation region. The pressure predicted by the modified model in the valley region is better, and this model not only captures the pressure peak accurately but also reveals a strong forward pressure gradient when $x/h > 7.5$.

The accuracy of the modified model in predicting the velocity and pressure coefficient outperforms that of the RANS model, and the friction coefficient is closely related to the fluid velocity dependent on the pressure field. Therefore, it can be seen in Fig. 13(b) that the modified model captures the wall friction coefficient more accurately than the original RANS model. The original RANS model predicts negative friction coefficients when $4.5 < x/h < 7$, while the predictions of the modified model are consistent with the results from LES. This is also because the reattachment point of the flow field computed by the original RANS model is delayed.

D. Prediction of the velocity for two massive separation flows

In order to explore the predictive performance of the higher-order discrepancy model, the previously trained model is directly

performed for the modification computation of the two massive separation periodic hill flows. The geometry used is illustrated in Fig. 14. The black geometry is the original size in this study, and the hill width is $k(y)$. The green and red represent the geometry of the hill width $\beta_1 k(y)$ and $\beta_2 k(y)$, respectively. The length of the bottom at the region for three geometries remains constant. Two massive separation flows at Re = 10 595 are simulated and modified, respectively, and the RMSE of the velocity for these two massive flows obtained is illustrated in Table IV. It can be seen that the velocity field obtained by the modified model is closer to the LES result by comparing the RMSE of the modified model and of the original RANS model with those of the LES. In order to intuitively compare the advantages of the modified model, the predictions of the velocity profiles obtained at different locations of two massive separated flows are given in Figs. 15 and 16.
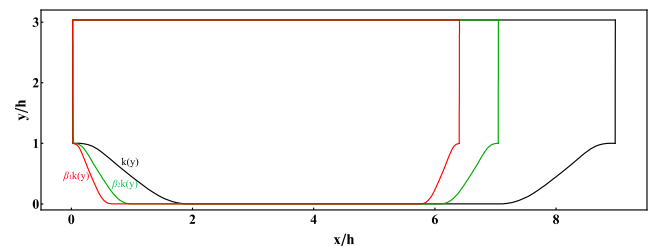

FIG. 14. The geometries of periodic hill flow with the original geometry shown in black, and the green and red represent the geometry of the hill width $\beta_1 k(y)$ and $\beta_2 k(y)$, respectively.

TABLE IV. RMSE of the velocity for two massive separated flow obtained by comparing the predicted results of the modified model and of the original RANS model with those of the LES.

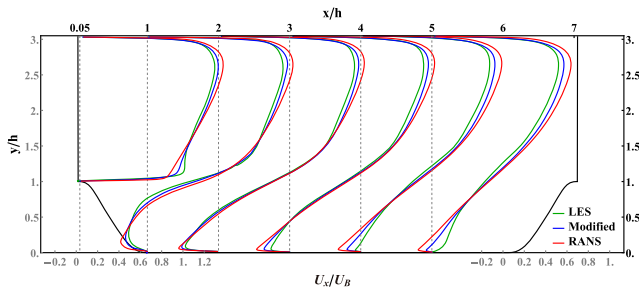| Massive separated flow	Modified model	RANS model
$\beta_1 k(y)$	0.056	0.091
$\beta_2 k(y)$	0.062	0.099

FIG. 15. Predictions of the mean x-direction velocity (U_x/U_B) profile for hill width $\beta_1 k(y)$ using the modified model compared with the predictions using LES and the original RANS model at Re $= 10\,595$.

FIG. 16. Predictions of the mean x-direction velocity (U_x/U_B) profile for hill width $\beta_2 k(y)$ using the modified model compared with the predictions using LES and the original RANS model at Re $= 10\,595$.
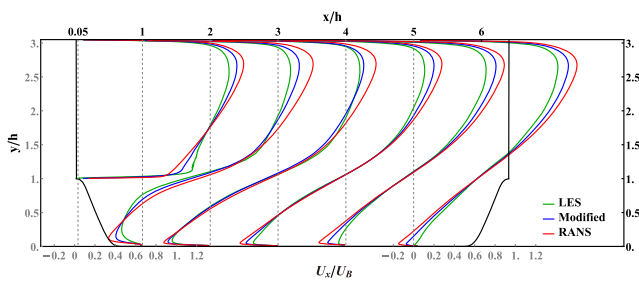
The hill width of the green geometry in Fig. 14 is $\beta_1 = 1/2$ times the original geometry. The trained discrepancy model used in case P2 is used to modify this massive separation flow. The modification results of mean x-direction velocity profiles is presented in Fig. 15, and it is shown that the results simulated by modified model and LES approach are more consistent in both trend and magnitude than the original RANS model and LES approach, which validate and verify whether the prediction of the modified model is still superior to the RANS model.

The red geometry in Fig. 14 has a greater slope with the hill width $\beta_2 k(y)$ ($\beta_2 = 1/3$). The modification computation for this massive separation flow is also derived from the trained discrepancy model used in case P2. The modification results in Fig. 16 show that the prediction accuracy of the modified model is still better than that of the original RANS model. However, the modified model is still not accurate enough to capture the reattached points.

E. Discussion

From the analysis of the results of interpolation and extrapolation modification, it can be seen that the modified model can capture the flow field phenomenon similar to the LES result better than the original RANS model. To further explore the generalization of the modified model. A greater degree of extrapolation of case P3 in Table V is performed. The flow at Re = 100 000 is modified. Meanwhile, a new case of ramp is also modified based on the discrepancy model trained in case P3. The specific results of the two modification computation are shown in Appendixes A and B, respectively.

Taghizadeh, Witherden, and Girimaji[36] proposed a closed loop training program that implements constraints in a self-consistent manner, which addresses the need for physical guidance in the development of machine learning-enhanced turbulence closure models. Their study points out three closure elements in the two-equation RANS model and also gives three key elements in machine learning modeling, namely, physical compatibility, training consistency, and loss function formulation, respectively. Based on the mentioned key elements, they incorporate the dynamics system into the training process to ensure consistency and compatibility among various coefficients. The meaningful and innovative method of Taghizadeh, Witherden, and Girimaji[36] inspired us to discuss the compatibility and consistency of the closure model based on the neural network.

The purpose of the machine learning-enhanced turbulence closure model is to hope that the prediction accuracy of the modified RANS model meets the requirements of high-fidelity data. Based on the above purpose, Ling, Kurzawski, and Templeton[13] obtains an improved Reynolds stress constitutive relationship through machine learning and replaces the original Reynolds stress term of the momentum equation with the trained Reynolds stress, which is a unidirectional transfer from the machine learning to the RANS equation solver. It is also the open loop training framework mentioned by Taghizadeh, Witherden, and Girimaji.[36] However, this method of explicit treatment of Reynolds stress has not significantly improved the prediction accuracy of the posterior velocity field. Therefore, in order to ensure the implicit treatment of Reynolds stress, the discrepancy in the anisotropic Reynolds stress between the high-fidelity data and the original RANS model is used to build a model in this study, and the discrepancy model is applied to modify the momentum equation and transport equation. In our training framework, the original transport closure coefficients are kept as unchanged as possible. Only the discrepancy of Reynolds stress is updated by the network, and the updated constitutive closure coefficients of the network are not used to modify the transport closure coefficients based on compatibility constraints. Therefore, the discrepancy model used in this study is not fully compatible.

TABLE V. Cases used for discrepancy model training and the original RANS model modification; RMSE of velocity for periodic hill (Re $= 100\,000$) and ramp (Re $= 10\,000$) obtained by comparing the predicted results of the modified model and the original RANS model with those of the LES.

| Cases | Datasets | | RMSE | |
	Discrepancy model training cases	Modification cases	Modified model	RANS model
P3	*Periodichill* : Re $= 2800, 5600, 8400, 10\,595$	*Periodichill* : Re $= 100\,000$	0.080	0.109
R1	*Periodichill* : Re $= 2800, 5600, 8400, 10\,595$	*Ramp* : Re $= 10\,000$	0.049	0.060

In order to improve the prediction accuracy of the posterior results, it is necessary to realize the bidirectional feedback transfer between the machine learning turbulence model and the RANS model solver. If the posterior result does not reach the prediction accuracy of the high-fidelity data, the modified result in the solver is fed back to the neural network, and the neural network starts to retrain and feeds back to the solver again. Through the iterative feedback between network training and the solver, the posterior accuracy of the RANS modified model achieves high fidelity, that is, the machine learning closed loop training framework is realized. This method overcomes the inconsistencies and incompatibility between various elements through iterative training and modification, so the computational cost of the closed loop framework will become higher.

Our research is not a completely closed loop model. However, compared to the open loop unidirectional prediction model of Ling, Kurzawski, and Templeton,[13] the discrepancy of Reynolds stress in the modified RANS model is solved iteratively by the network in real time, which is similar to a semi-closed-loop training framework. The initial state modeled in this paper is consistent with the ideal state of closed loop iterative modification. That is, the posterior flow field of the modified RANS model has achieved high-fidelity data accuracy. Therefore, the input and output of the neural network all come from high-fidelity data. The network training is performed based on the high-order model and then fed back to the solver. The solver realizes semi-implicit treatment of the Reynolds stress. The closed loop training framework proposed by Taghizadeh, Witherden, and Girimaji[36] provides an improvement goal and direction for this study.

V. CONCLUSIONS

In the study of the typical data-driven Reynolds stress model, high-fidelity Reynolds stress data as source terms are treated completely explicitly to solve the RANS equation. The mean velocity field results obtained by this approach are not ideal. In this paper, a semi-implicit treatment of the Reynolds stress anisotropy discrepancy model is derived using a higher-order tensor basis with the aim of improving the prediction accuracy of the mean velocity. A DNN is constructed to train this discrepancy model based on the periodic hill flow at different Reynolds numbers. In this approach, the

Reynolds stress term is not completely replaced, thereby ensuring the implicit solution of the Reynolds stress in the RANS equation, and the relaxation coefficient ensures the convergence of the model as well.

First, interpolation modifications are performed based on the Reynolds number. The modified model is then explored further regarding its prediction capability by modifying the medium-Reynolds-number flow fields. When performing modification, the ability to capture anisotropic features and turbulent states in triangles of the modified model have been improved compared with the original RANS model. In addition, the modified model is also able to accurately predict the mean velocity profile. For the modified model, the values of the RMSE compared with the LES results are 0.048 and 0.046, respectively, for two cases, which are significantly lower than the corresponding RMSE values for the original RANS model (0.081 and 0.064). Besides, the modified model improves the prediction accuracy for the mean pressure coefficient and mean friction coefficient of the underlying wall surface compared with the original RANS model. In particular, the pressure peaks and friction peak are more accurately captured; meanwhile, the prediction of the recirculation region and the reattachment point have also been improved. The above results show that the semi-implicit treatment of Reynolds stress makes the model converge well as well as improve the prediction accuracy, and thus, it would be more applicable for industrialization.

Future work needs to examine the scope for generalizing the modified RANS model, and we are planning to apply it to more complex multiphase flows, such as cavitation flows and flows in complex geometries. In addition, we will investigate the possibilities of using the turbulence model coupled with the cavitation phase transition to simulate the time-varying instability of cavitation flow with an acceptable computational cost.
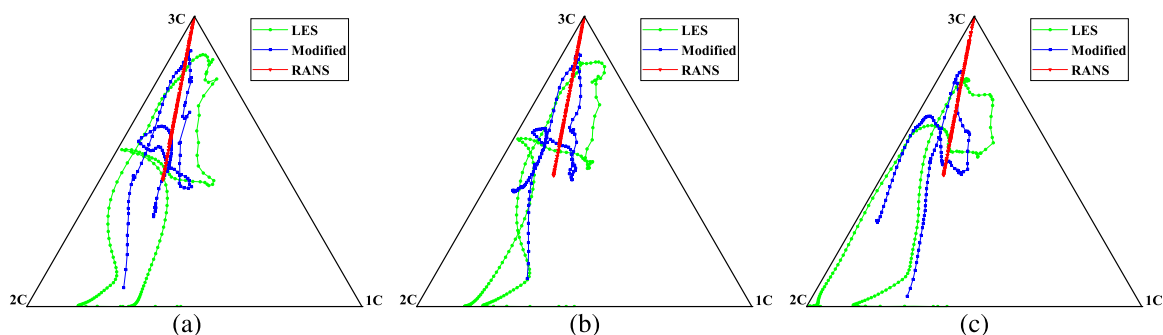
ACKNOWLEDGMENTS

FIG. 17. Prediction performance for the Reynolds stress anisotropy for the case (Re = 100 000) using LES, the modified model, and the original RANS model at three locations (x/h = 2, 4, 6), plotted as barycentric maps with (a) x/h = 2, Re = 100 000; (b) x/h = 4, Re = 100 000; and (c) x/h = 6, Re = 100 000.
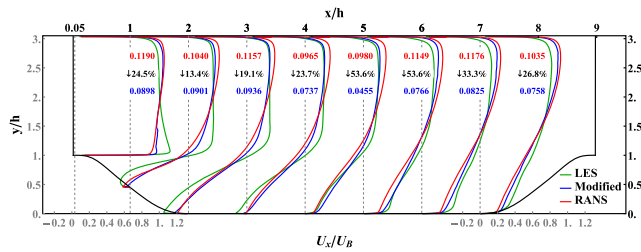
FIG. 18. Predictions of the mean x-direction velocity (U_x/U_B) profile using the modified model compared with the predictions using LES and the original RANS model at Re = 100 000. The blue and red numbers are the RMSE values from the modified model and the original RANS model, respectively, and the black numbers are the deviation reduction.
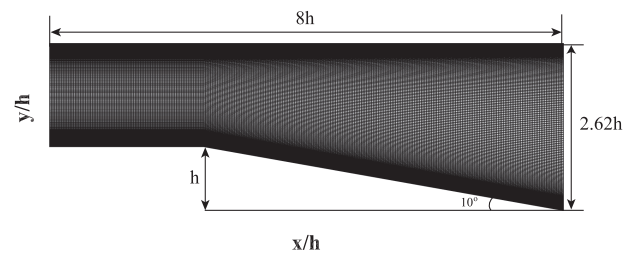

FIG. 19. Computation domain for the ramp.

APPENDIX A: PREDICTION UNDER A GREATER DEGREE OF EXTRAPOLATION MODIFICATION

To further explore the generalization of the modified model in a high-Reynolds-number flow field, a greater degree of extrapolation of case P3 in Table V is performed. The flow at Re = 100 000 is modified. Figure 17 presents the Reynolds stress anisotropy for the case of Re = 100 000. It can be seen that the modified model is still superior to the original RANS model in capturing the anisotropy of the Reynolds stress with a greater degree of Reynolds number. Figure 18 shows that the velocity prediction accuracy of the modified model is not significantly improved compared with LES but

is better than that of the original RANS model. The RMSE for the modified model compared with the LES result is 0.080, which is significantly lower than the corresponding RMSE values for the original RANS model (0.109). Therefore, the constructed Reynolds stress discrepancy model not only has satisfactory prediction performance for the low Reynolds and medium Reynolds numbers but also has better prediction accuracy for a greater degree of Reynolds numbers than the original RANS model.

APPENDIX B: RAMP

In order to verify the applicability of the modified model, in addition to the interpolation and extrapolation modification based on the Reynolds number, a modification computation of 2D ramp
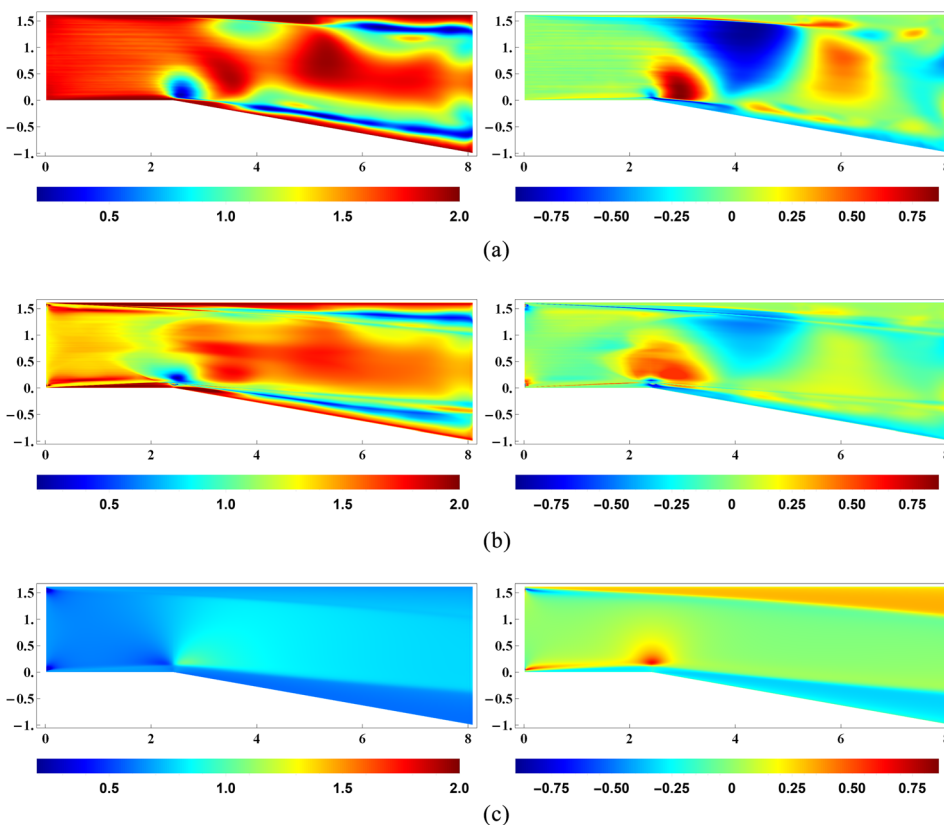

(a)

(b)

(c)

FIG. 20. Predictions for the Reynolds stress $\overline{u'_1 u'_1}/k$ and $\overline{u'_1 u'_2}/k$ obtained by (a) LES, (b) the modified model, and (c) the original RANS model.
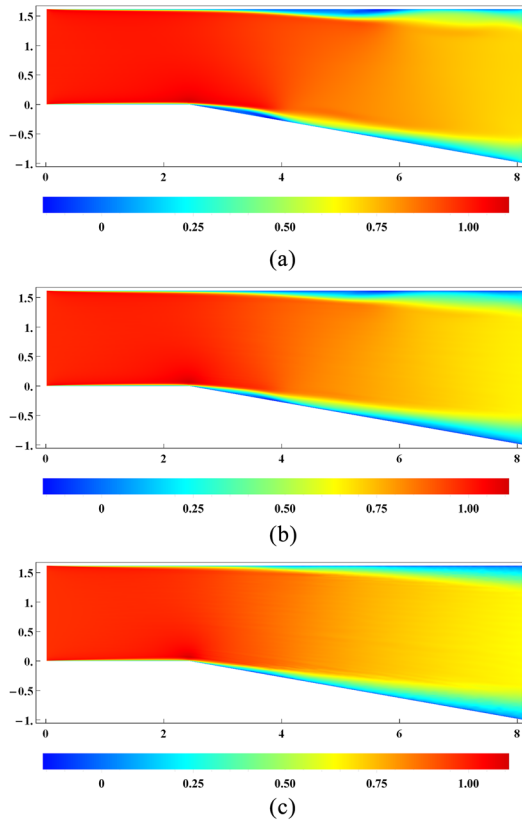
FIG. 21. Predicted mean velocity (U_x/U_B) contours simulated by (a) LES, (b) the modified model, and (c) the original RANS model.

is also carried out. The computation domain is shown in Fig. 19, which extends $8h$ along the x direction, and its left side is the velocity entrance with a height of $1.62h$, where h is the height of the diffusion section. The corner of the diffuser is $10°$. The 2D RANS model is used for baseline simulation, the inlet velocity is $U_B = 10$ m/s, and the Reynolds number is 10^4.

Using the training model corresponding to $P3$ in Table V, combined with the modification method in Sec. II B, the 2D ramp is modified. The predictions for the Reynolds stress $\overline{u_1'u_1'}/k$ and $\overline{u_1'u_2'}/k$ simulated by LES, the modified model, and the original RANS model are presented in Fig. 20. Compared with the RANS model, the prediction accuracy of the modified model for Reynolds stress is closer to the LES result. The improved prediction accuracy of the modified model is manifested in the separation of the flow field on the lower wall and the flow field characteristics of the upper wall are captured.

The velocity field is solved using the modified Reynolds stress, and the result of the mean velocity contour is shown in Fig. 21(b). In comparison with the target velocity data obtained by LES, the RMSE was computed by our modified model as 0.049, which is significantly lower than the RMSE computed by the original RANS model (0.060). Meanwhile, compared with the results of LES and the original RANS model [see Figs. 21(a) and 21(c)], it can be seen that when $2.5 < x < 6$, the prediction performance of the velocity field obtained by the modified model is most significant. Therefore, this paper continues to analyze the predi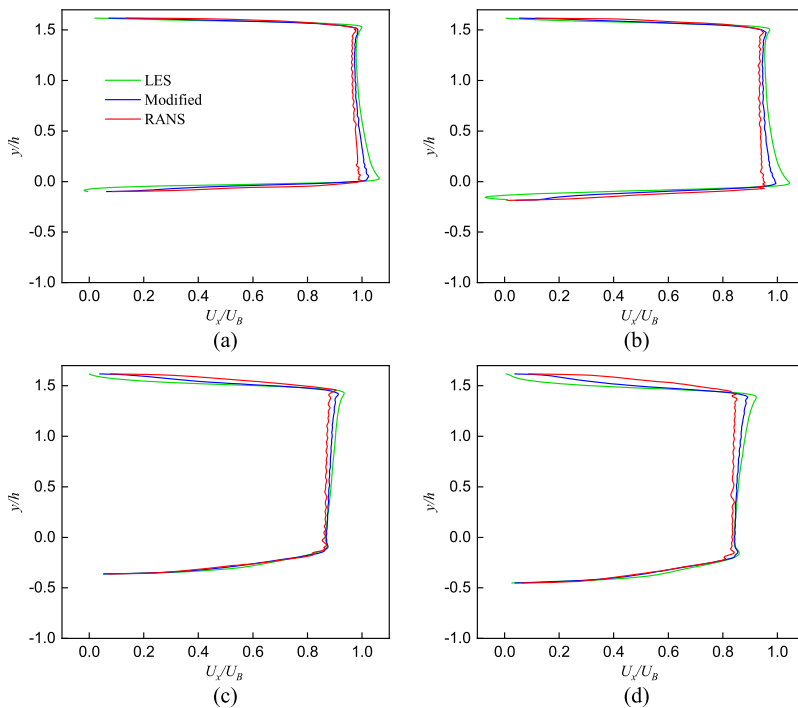ction results of the velocity profiles. Figure 22 demonstrates the predictions of the mean x-direction velocity (U_x/U_B) profiles using the modified model compared with the predictions using LES and the original RANS model at four different locations ($x/h = 3$, 3.5, 4.5, and 5). It can be seen from the profile curves at four locations that the results of the modified model are in better agreement

FIG. 22. Predictions of the mean x-direction velocity (U_x/U_B) profiles using the modified model compared with the predictions using LES and the original RANS model at four different locations ($x/h = 3$, 3.5, 4.5, and 5) with (a) $x/h = 3$, (b) $x/h = 3.5$, (c) $x/h = 4.5$, and (d) $x/h = 5$.

with the results of the LES model than those of the original RANS model.

DATA AVAILABILITY

The data that support the findings of this study are available from the corresponding author upon reasonable request.

REFERENCES

[1]W. Rodi, "On the simulation of turbulent flow past bluff bodies," J. Wind Eng. Ind. Aerodyn. **46-47**, 3–19 (1993).

[2]P. R. Spalart, "Philosophies and fallacies in turbulence modeling," Prog. Aerosp. Sci. **74**, 1–15 (2015).

[3]B. E. Launder and B. I. Sharma, "Application of the energy-dissipation model of turbulence to the calculation of flow near a spinning disc," Lett. Heat Mass Transfer **1**, 131–137 (1974).

[4]P. R. Spalart, "A one-equation turbulence model for aerodynamic flows," AIAA Paper No. 92-0429, 1992.

[5]F. R. Menter, "Two-equation eddy-viscosity turbulence models for engineering applications," AIAA J. **32**, 1598–1605 (1994).

[6]P. E. Hamlington and W. J. A. Dahm, "Reynolds stress closure for nonequilibrium effects in turbulent flows," Phys. Fluids **20**, 115101 (2008).

[7]P. E. Hamlington and M. Ihme, "Modeling of non-equilibrium homogeneous turbulence in rapidly compressed flows," Flow, Turbul. Combust. **93**, 93–124 (2014).

[8]T. B. Gatski and C. G. Speziale, "On explicit algebraic stress models for complex turbulent flows," J. Fluid Mech. **254**, 59–78 (1993).

[9]S. L. Brunton, B. R. Noack, and P. Koumoutsakos, "Machine learning for fluid mechanics," Annu. Rev. Fluid Mech. **52**, 477–508 (2020).

[10]Y. Yin, P. Yang, Y. Zhang, H. Chen, and S. Fu, "Feature selection and processing of turbulence modeling based on an artificial neural network," Phys. Fluids **32**, 105117 (2020).

[11]M. Yang and Z. Xiao, "Improving the k–ω–γ–A_r transition model by the field inversion and machine learning framework," Phys. Fluids **32**, 064101 (2020).

[12]K. Duraisamy, G. Iaccarino, and H. Xiao, "Turbulence modeling in the age of data," Annu. Rev. Fluid Mech. **51**, 357–377 (2019).

[13]J. Ling, A. Kurzawski, and J. Templeton, "Reynolds averaged turbulence modelling using deep neural networks with embedded invariance," J. Fluid Mech. **807**, 155–166 (2016).

[14]J. X. Wang, J. L. Wu, and H. Xiao, "Physics informed machine learning approach for reconstructing Reynolds stress modeling discrepancies based on DNS data," Phys. Rev. Fluids **2**, 034603 (2017).

[15]R. Maulik and O. San, "A neural network approach for the blind deconvolution of turbulent flows," J. Fluid Mech. **831**, 151–181 (2017).

[16]B. Kim, V. C. Azevedo, N. Thuerey, T. Kim, M. Gross, and B. Solenthaler, "Deep fluids: A generative network for parameterized fluid simulations," Comput. Graphics Forum **38**, 59–70 (2019).

[17]S. Pan and K. Duraisamy, "Data-driven discovery of closure models," SIAM J. Appl. Dyn. Syst. **17**, 2381–2413 (2018).

[18]S. Pawar, S. M. Rahman, H. Vaddireddy, O. San, A. Rasheed, and P. Vedula, "A deep learning enabler for nonintrusive reduced order modeling of fluid flows," Phys. Fluids **31**, 085101 (2019).

[19]B. Liu, J. Tang, H. Huang, and X.-Y. Lu, "Deep learning methods for super-resolution reconstruction of turbulent flows," Phys. Fluids **32**, 025105 (2020).

[20]L. Zhu, W. Zhang, J. Kou, and Y. Liu, "Machine learning methods for turbulence modeling in subsonic flows around airfoils," Phys. Fluids **31**, 015105 (2019).

[21]J. Ling and J. Templeton, "Evaluation of machine learning algorithms for prediction of regions of high Reynolds averaged Navier Stokes uncertainty," Phys. Fluids **27**, 085103 (2015).

[22]J. Ling, A. Ruiz, G. Lacaze, and J. C. Oefelein, "Uncertainty analysis and data-driven model advances for a jet-in-crossflow," J. Turbomachinery **139**, 021008 (2017).

[23]J. Ling, R. Jones, and J. Templeton, "Machine learning strategies for systems with invariance properties," J. Comput. Phys. **318**, 22–35 (2016).

[24]S. B. Pope, "A more general effective-viscosity hypothesis," J. Fluid Mech. **72**, 331–340 (1975).

[25]Z. Zhang, X.-d. Song, S.-r. Ye, Y.-w. Wang, C.-g. Huang, Y.-r. An, and Y.-s. Chen, "Application of deep learning method to Reynolds stress models of channel flow based on reduced-order modeling of DNS data," J. Hydrodyn. **31**, 58–65 (2019).

[26]M. Gamahara and Y. Hattori, "Searching for turbulence models by artificial neural network," Phys. Rev. Fluids **2**, 054604 (2016).

[27]S. Pawar, O. San, A. Rasheed, and P. Vedula, "A priori analysis on deep learning of subgrid-scale parameterizations for Kraichnan turbulence," Theor. Comput. Fluid Dyn. **34**, 429 (2020).

[28]A. Beck, D. Flad, and C.-D. Munz, "Deep neural networks for data-driven LES closure models," J. Comput. Phys. **398**, 108910 (2019).

[29]J. Weatheritt and R. Sandberg, "A novel evolutionary algorithm applied to algebraic modifications of the RANS stress-strain relationship," J. Comput. Phys. **325**, 22–37 (2016).

[30]R. Maulik, O. San, J. D. Jacob, and C. Crick, "Sub-grid scale model classification and blending through deep learning," J. Fluid Mech. **870**, 784–812 (2019).

[31]H. Xiao, J. L. Wu, J. X. Wang, and E. G. Paterson, "Are discrepancies in RANS modeled Reynolds stresses random?," arXiv:1606.08131 (2016).

[32]J. Wu, H. Xiao, and E. G. Paterson, "Physics-informed machine learning approach for augmenting turbulence models: A comprehensive framework," Phys. Rev. Fluids **3**, 074602 (2018).

[33]J. Wu, H. Xiao, R. Sun, and Q. Wang, "Reynolds-averaged Navier–Stokes equations with explicit data-driven Reynolds stress closure can be ill-conditioned," J. Fluid Mech. **869**, 553–586 (2019).

[34]D. C. Wilcox, "Formulation of the k–ω turbulence model revisited," AIAA J. **46**, 2823–2838 (2008).

[35]S. B. Pope, *Turbulent Flows* (Cambridge University Press, 2000).

[36]S. Taghizadeh, D. F. Witherden, and S. S. Girimaji, "Turbulence closure modeling with data-driven techniques: Physical compatibility and consistency considerations," New J. Phys. **22**, 093023 (2020).

[37]D. Li and H. Christian, "Simulation of bubbly flows with special numerical treatments of the semi-conservative and fully conservative two-fluid model," Chem. Eng. Sci. **174**, 25–39 (2017).

[38]L. F. L. R. Silva and P. L. C. Lage, "Development and implementation of a polydispersed multiphase flow model in OpenFOAM," Comput. Chem. Eng. **35**, 2653–2666 (2011).

[39]A. L. Maas, A. Y. Hannun, and A. Y. Ng, "Rectifier nonlinearities improve neural network acoustic models," in *International Conference on Machine Learning (ICML)* (Association for Computing Machinery, New York, NY, 2013).

[40]A. Krogh and J. Hertz, "A simple weight decay can improve generalization," in *International Conference on Neural Information Processing Systems* (MIT Press, Cambridge, MA, 1992), Vol. 4, pp. 950–957.

[41]M. Breuer, N. Peller, C. Rapp, and M. Manhart, "Flow over periodic hills—Numerical and experimental study in a wide range of Reynolds numbers," Comput. Fluids **38**, 433–457 (2009).

[42]N. Peller and M. Manhart, "Turbulent channel flow with periodic hill constrictions," in *New Results in Numerical and Experimental Fluid Mechanics*, Lecture Notes on Numerical Fluid Mechanics and Multidisciplinary Design (NNFM) Vol. 92, edited by H. J. Rath, C. Holze, H. J. Heinemann, R. Henke, and H. Hönlinger (Springer, 2006), pp. 504–512.

[43]J. Fröhlich, C. P. Mellen, W. Rodi, L. Temmerman, and M. A. Leschziner, "Highly resolved large-eddy simulation of separated flow in a channel with streamwise periodic constrictions," J. Fluid Mech. **526**, 19–66 (2005).

[44]L. Temmerman and M. A. Leschziner, "Large eddy simulation of separated flow in a streamwise periodic channel construction," in *International Symposium on Turbulence and Shear Flow Phenomena* (Association for Computing Machinery, New York, NY, 2001), pp. 399–404.

[45]A. Yoshizawa, "Statistical theory for compressible turbulent shear flows, with the application to subgrid modeling," Phys. Fluids **29**, 2152–2164 (1986).

[46]C. Rapp, F. Pfleger, and M. Manhart, "New experimental results for a LES benchmark case," in *Direct and Large-Eddy Simulations VII*, edited by V. Armenio, B. Guerts, and J. Fröhlich (Springer, 2009), pp. 69–74.

[47]S. Banerjee, R. Krahl, F. Durst, and C. Zenger, "Presentation of anisotropy properties of turbulence, invariants versus eigenvalue approaches," J. Turbul. **8**, N32 (2007).